Supplemental Material: Phase-tuned entangled state generation between distant spin qubits

R. Stockill,[1] M. J. Stanley,[1] L. Huthmacher,[1] E. Clarke,[2] M. Hugues,[3]
A. J. Miller,[4] C. Matthiesen,[1, *] C. Le Gall,[1] and M. Atatüre[1, †]

[1]*Cavendish Laboratory, University of Cambridge,*
JJ Thomson Avenue, Cambridge CB3 0HE, UK
[2]*EPSRC National Centre for III-V Technologies,*
University of Sheffield, Sheffield, S1 3JD, UK
[3]*Université Côte d'Azur, CNRS, CRHEA, rue Bernard Grégory, 06560 Valbonne, France*
[4]*Quantum Opus, LLC, 45211 Helm St., Plymouth, MI 48170, USA*

ORIGIN AND CONTROL OF THE ENTANGLED STATE PHASE IN A SINGLE-PHOTON ENTANGLEMENT SCHEME

Phase of the entangled state

Upon detection of a Raman photon, the phase of the entangled state is given by $\Delta\phi$, a function of the blue and red frequencies (ω_B, ω_R), the time interval it takes for the light to travel from the first beam splitter to QD_A and QD_B ($t_{1,A}$ and $t_{1,B}$) and the time interval it takes to travel from the QDs to the detector that registers the Raman-photon click after the second beam splitter ($t_{2,A}$ and $t_{2,B}$):

$$\Delta\phi = \omega_R(t_{1,A} - t_{1,B}) + \omega_B(t_{2,A} - t_{2,B}) + \omega_{\mathrm{Larmor}}(t_{3,A} - t_{3,B}) \tag{1}$$

Here we also include the phase acquired in the tomography step which can be expressed as a function of the Larmor frequency ω_{Larmor} and the time interval between the Raman photon click and the spin rotation at QD_A and QD_B ($t_{3,A}$ and $t_{3,B}$). We note that in our experimental configuration, these times are negative as the spin rotation pulses arrive before the Raman photon click. Equation 1 encompasses all the experimental requirements to measure the entanglement. First, the interferometer phase must be stable in order to select a single entangled state. In addition, the Mach-Zehnder interferometer must be arranged such that $t_{2,A} + t_{3,A} = t_{2,B} + t_{3,B}$ in order that we may identify the phase of the Rayleigh-scattered photons with a consistent entangled state. This ensures that the tomography phase cancels the optical phase accumulated if the Mach-Zehnder is asymmetric ($t_{1,A} \neq t_{1,B}$) and/or longer along one of the two QD paths ($t_{1,A} + t_{2,A} \neq t_{1,B} + t_{2,B}$). Stability of the interferometer delay and phase cancelling by the spin rotation delay should all be controlled to well within the 40 ps of Larmor precession if one is to create and measure an entangled state with a well defined phase.

In practice, we set the Mach-Zehnder working point around the zero delay position ($< \pm 0.15$ ps), and ensure that the spin-rotation pulses arrive at each QD with delay such that their reflections reach the second Mach-Zehnder beam splitter simultaneously ($< \pm 0.5$ ps). This is achieved by monitoring the interferograms of continuous wave lasers at the QD resonance frequencies and the interference of the scattered spin rotation pulses.

Phase Stabilization

The phase of the Mach-Zehnder interferometer in this experiment is monitored with a far-detuned phase-reference laser at 956nm, where a relative phase $\Delta\phi_{\mathrm{Ref}}$ is accumulated between the two paths. This laser enters the interferometer at the first beam splitter and follows the same path as that of the entanglement pulse and Raman-scattered photon mode. Due to the highly chromatic nature of the polarization-based background suppression we reject lasers at the QD resonance frequency while detecting count rates of ≈ 1.5 MHz per QD at the phase-reference frequency. This signal is filtered from the QD frequencies at each interferometer output by 1200 lines/mm gratings and detected on two silicon single photon counting modules (SPCM). Pulse counters convert the detection event rates to two analog signals which are subtracted to generate an error signal for a PID system (SRS SIM960). Such balanced detection of the two beam splitter outputs reduces the impact of laser and background suppression-related intensity noise. In Fig. S1(a) we present the interference fringes recorded for a 30-s running time. Both slow phase wander and audio-frequency noise contribute in the free-running case. A retroreflector mounted on a 300-μm travel piezo-driven stage is incorporated into the interferometer to follow the slow drift, while a phase electro-optic modulator compensates for audio-frequency noise.

We define $\Delta\phi_i$ as the phase accumulated through the Mach-Zehnder interferometer by light propagating at a frequency ω_i, where $i = B, R, \mathrm{Ref}$ refers to the blue, red or phase-reference frequencies respectively.
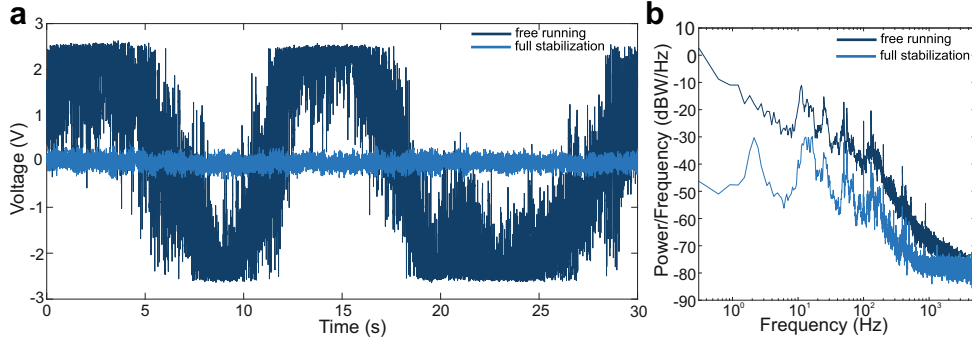
FIG. S1: (a) Phase-reference output difference for free-running (dark blue) and stabilized (light blue) interferometer. The SPCM count rates have been converted to an analogue voltage. Fitting the stabilized signal reveals a FWHM of 6.8 degrees. (b) Power spectral density for the free-running and the stabilized interferometer (dark blue and light blue respectively).

In Fig. S1(b) the fast Fourier transform (FFT) of the signal from the phase reference is given in the free-running and actively stabilized cases. Noise reduction is measurable for frequencies up to ≈ 1.5 kHz, corresponding to the detection bandwidth (set by the pulse counter bandwidth). The overall power in the integrated spectrum is reduced by a factor 260, and the phase is stabilized around a set angle shown in Fig. S1(a) with a FWHM of $6.8°$. The operating setpoint of the stabilization-loop is $\Delta\phi_{\mathrm{Ref}} = \pi/2$, which yields a linear error signal and mitigates uncorrelated intensity drifts from each cryostat output. Introducing a small delay in one interferometer arm (≤ 0.3 ps) allows us to choose an arbitrary phase for the blue frequency ($\Delta\phi_B \in [0, \pi]$), while stabilizing at $\Delta\phi_{\mathrm{Ref}} = \pi/2$ and maintaining the interference at the blue and red frequencies effectively in phase ($|\Delta\phi_R - \Delta\phi_B| \leq 3°$).

Interference from Rayleigh scattering

In Fig. S2 we present the effect of the phase stabilization on QD Rayleigh scattering. The Figure shows the count rates observed at the two red-frequency outputs of the interferometer during the 1.2-ns entanglement window, with a 0.5-s integration time. Rayleigh-scattered photons from the two distant QDs are phase coherent and present interference fringes at the output of the second beam splitter. For the first 70 seconds the phase of the interferometer is free-running and the two outputs beat against each other with a π-phase shift. After 70 seconds we stabilize the interferometer phase and the fluorescence from the two QDs is predominantly directed towards output one. The visibility, V, observed in the course of the experiment typically lies at 65%.

The visibility of the interference stemming from Rayleigh scattering provides information on the quality of the path interference central to the entanglement scheme used here. The finite power of the excitation pulse (inducing a Raman process with 5.9% probability for $\mathrm{QD_A}$ and 7.9% for $\mathrm{QD_B}$) leads to a small amount of incoherent emission at the red frequency (which we estimate to contribute 11% for $\mathrm{QD_A}$ and 15% for $\mathrm{QD_B}$), resulting in an expected visibility of $V = 75\%$ for the case of ideal Λ-systems. As stated in the manuscript, a drop of visibility by 4% is caused by the imperfect mode overlap. A further drop by $\approx 10\%$ is most likely caused by nuclear and electric-field noise on microsecond to second timescales [1–3], which detunes the resonances of the QDs by δ from shot to shot. This detuning in turn creates a phase shift of the Rayleigh scattering process, analogous to the detuning-dependent phase shift of a driven damped harmonic oscillator. The phase shift here, rather than evolving rapidly on a detuning range given by the width of the transition as in a CW case, changes over a detuning range of $2/T_{\mathrm{p}} \approx 10\Gamma$, where T_{p} is the duration of the entanglement pulse and Γ the excited-state decay rate. Averaging over an
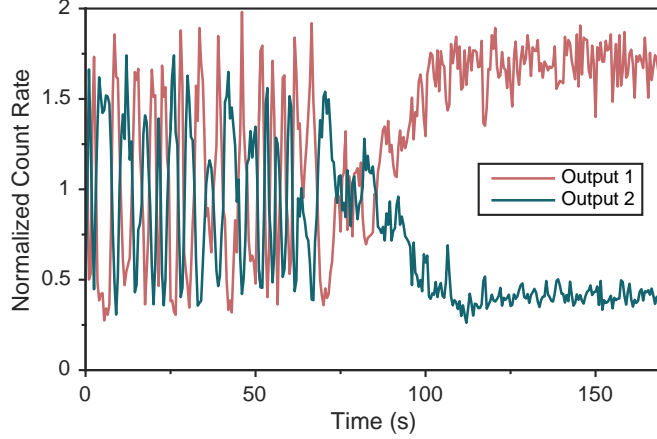
FIG. S2: Time-averaged Rayleigh-scattering interference from the two QDs during the state-projection pulse. For the first 70 seconds the interferometer is free running. After that point the phase is stabilized.

integration time of 0.5 s we observe a reduction in the visibility. We estimate from a numerical simulation that the intrinsic noise $(\delta_{\mathrm{nuc}})_{\mathrm{FWHM}} = 50$ MHz due to hyperfine coupling has a small effect ($\Delta V < 1\%$). Extrinsic electric-field noise on the order of $(\delta_{\mathrm{elec}})_{\mathrm{FWHM}} = 300 - 500$ MHz on shorter timescales than the integration time is the main source for the drop in visibility observed here, which will directly affect the visibility in the rotated basis of the two spins.

PULSE SEQUENCE

Creating and characterizing entanglement between distant electron spins requires multiple distinct processes to prepare, project, control and read-out the spins of the two QDs. These requirements are fulfilled by four optical sources. The read-out, preparation and entanglement pulses are formed from CW semiconductor-diode lasers by electro-optic modulators with a 1.7 GHz bandwidth for preparation and read-out pulses and 20 GHz bandwidth for entanglement pulses. The spin control is provided by red-detuned picosecond pulses from a modelocked Ti:Sapphire source (Coherent MIRA 900). We correlate spin measurements by passing the detector outputs to a time-to-digital converter (TDC - Qutools quTAU). This allows us to partition detection events into 81-ps time bins, which we compare to the pulse sequence clock.

The modelocked laser provides a ≈ 76 MHz clock. We create the control sequences employing the hardware configuration shown in Fig. S3 to synchronize the various pulses together. This process can be partitioned into three distinct sections for timing, spin projection/read-out and pulse picking coherent control pulses. A Tektronix 70002A Arbitrary Waveform Generator (AWG) mediates the three sections. The components are covered in more detail below.

Timing

In order to synchronize our control sequence we take a pick-off of the modelocked source and amplify the detected signal to gain an electrical reference. We split this signal into two and filter one output to provide a 76 MHz reference clock for the AWG. The other half is pre-scaled by a factor of 360 using a Stanford Research Systems DG645 Digital Delay Generator to provide a trigger for starting the pulse sequence. One output of the AWG provides a single pulse every 52 repetitions of the entanglement
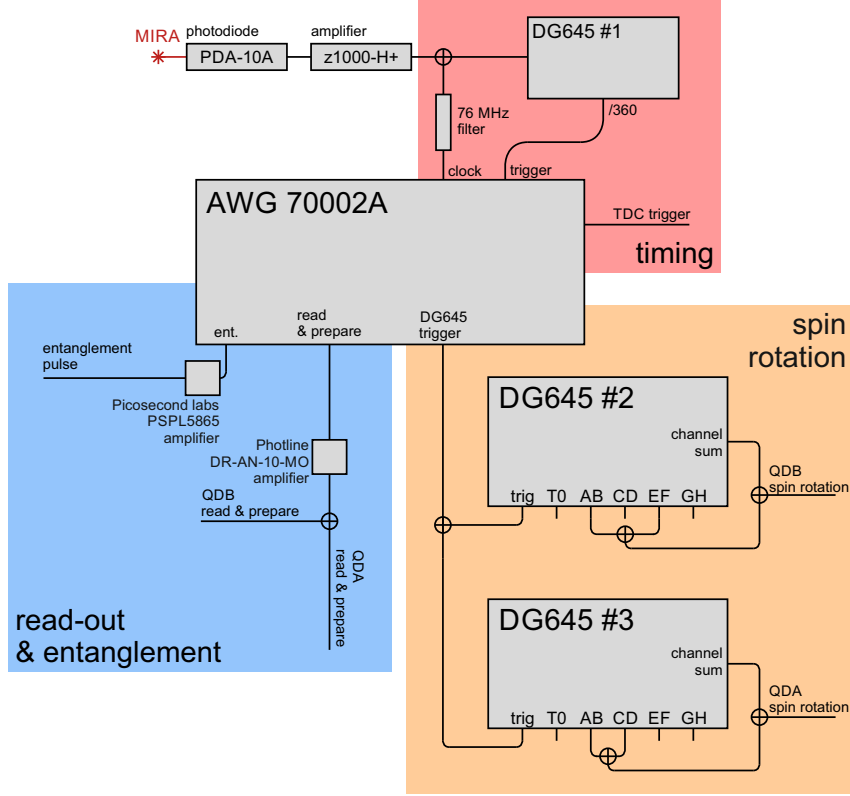
FIG. S3: Schematic of equipment for the spin-spin entanglement pulse sequence. The setup can be divided into three main parts: responsible for the overall timing, the modulation of spin read-out and entanglement pulses, and the pulse picking of the modelocked laser for coherent spin rotations.

sequence (~ 0.2 MHz), which we send to the TDC to correlate photon detection events from the two QDs.

Read-out & Entanglement

We form the spin preparation, entanglement and read-out pulses using fibre-based LiNbO$_3$ waveguide electro-optic modulators. The modulators are driven by square pulses formed by the AWG, which we amplify to provide maximum contrast in the interferometric modulator output. We compensate against thermal drift in the waveguides through active feedback to a DC-offset. In this way we reliably achieve on-off ratios of > 300 such that spin populations are long-lived in the absence of a read-out pulse.

The 160-ps entanglement pulses are created from a single diode laser, resonant with the red transition in the two QDs. The pulses are distributed to the two QDs by the first beam splitter of the interferometer (see Fig. 1 of main text) to ensure phase-coherent excitation. A diode laser for each QD resonant with the blue transition provides both the 7-ns state read-out and 20-ns spin preparation pulses. A relative delay in the pulse pattern for each cryostat allows us to distinguish spin read-out fluorescence between the two QDs.
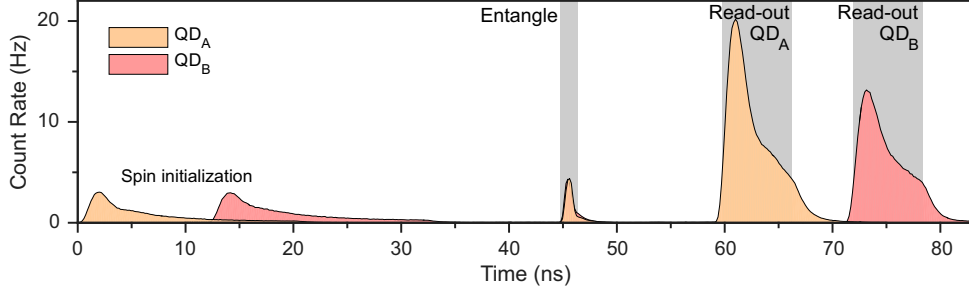
FIG. S4: Two-QD pulse sequence fluorescence. The fluorescence from each QD is recorded separately and superimposed. Visible are the spin initialization, entanglement and spin read-out pulses for each QD. The altered shape of the entanglement pulse compared to Fig. 2 of the main text is due to the presence of the spin rotation pulse arriving 1.2 ns after the weak excitation, detuning the QD emission outside of the detection frequency window.

Control

Tomography of the projected state requires independent rotation of the two electron spins. The picosecond pulses we use for the coherent rotations are red-detuned from the exciton transitions by ~ 3 nm. We first split and recombine the pulsed laser in an unstabilized Michelson interferometer featuring a 40-ps delay to form composite rotation pairs (see the discussion of 'Single Quantum Dot Spin Recovery' below). The two outputs of the interferometer then provide the control pulses for each spin. We pick the required pulses for each QD using one of two free-space acousto-optic modulators (AOMs - AA MT350). We drive each modulator with combined pulses from a digital delay generator triggered by an AWG output. The variable height of the pulses allows us to choose between $\pi/2$, π and $3\pi/2$ rotations. Finally, a lower frequency AOM (AAMT80) driven by a PID loop stabilizes the average power reaching each cryostat to ensure constant angle rotations during each measurement.

PULSE SEQUENCE FLUORESCENCE

Figure S4 displays the time-averaged fluorescence during the entanglement pulse sequence correlated with the sequence clock. The signal from each QD is recorded separately by blocking one arm of the Mach-Zehnder interferometer. The regions of interest for finding three-photon coincidences are highlighted as the grey filled rectangles. The low amplitude decays at the beginning of the sequence are due to the spin-initialization pulses for each QD. The peak at ∼46 ns is the entanglement pulse due to weak excitation of the QDs. The spin rotation occurs at the end of this pulse (at 47 ns), not visible here owing to the lack of photons generated during this step. The exponential decays starting at 60 and 72 ns stem from the state read-out pulses for each QD. The decaying fluorescence follows the repumping of the spin occuring during read-out. For the read-out pulses we drive each transition at saturation intensity to maximise the photon rate without introducing large amounts of background scatter from the probe laser to our signal. This generates an average of 1.6 photons for a 'bright' spin state $|\uparrow\rangle$.

SINGLE QUANTUM DOT SPIN RECOVERY

Here we quantify the fidelity of projecting and retrieving a spin state from each QD. If we run the entanglement sequence and block one arm of the Mach-Zehnder interferometer, a Raman-photon detection
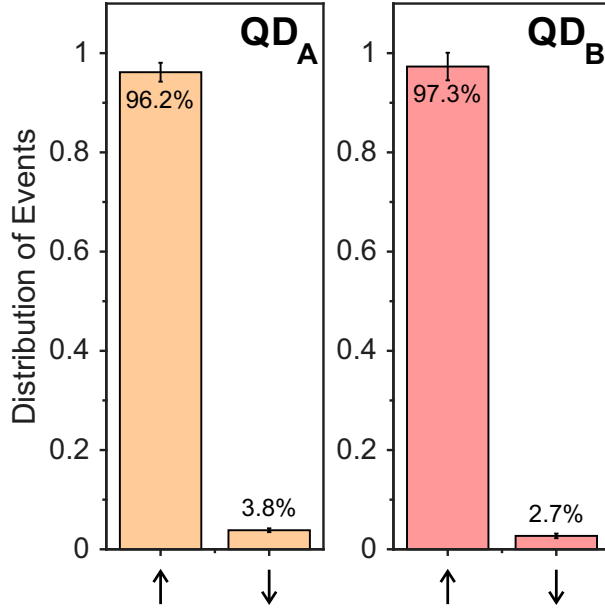
FIG. S5: Raman photon spin heralding. Proportion of conditional spin-read-out events arranged according to basis state for QD$_A$ and QD$_B$. The error bars mark the shot-noise limited uncertainty in the proportion.

event heralds a spin-up population in the single QD.

To test this heralding and recovery, we correlate the spin read-out on the detection of a Raman photon. The distribution of two-photon coincidences for each QD is displayed in Fig. S5. Conditioning on a Raman photon detection event predicts a spin-up population to a high probability. We project and retrieve a spin-up population with a fidelity of 96.2±1.9% for QD$_A$ and 97.3±2.7% for QD$_B$. This figure, set by the fidelity of our π spin rotation, the filtering of our Raman mode from the spin-conserving Rayleigh scattering and the rejection of stray laser light, provides an upper bound for the fidelity of our spin-state recovery in the main text. At the same time, we note that this figure is not sensitive to the fidelity of our spin initialization, nor does it measure stray spin-pumping between the π spin rotation and the state read-out. The former is confirmed to provide $< 5\%$ error in our two-QD measurement. The latter, set by the imperfect modulator suppression of the read-out pulse, is estimated to reduce our total coincidence rate by $\sim 1\%$, but does not change the distribution of coincidences and therefore does not affect the entangled state fidelity we measure.

Accurate tomography requires high-fidelity rotations of each confined spin. Precession in the external magnetic field during our few-picosecond rotation tilts our rotation axis away from the Bloch-sphere equator and prevents us from completely inverting the spin with a single pulse. For the measurement presented in Fig. S5 and the joint spin tomography in the main paper we rotate the spins with pairs of pulses, separated by slightly less than a free-precession period. In the case of a π rotation, this requires a composite pair of $\sim \pi/2$ rotations [4]. For comparison, with a single optical rotation the single-spin retrieval fidelity is limited to $\sim 92\%$ owing to a 12.5° tilt in our rotation axis induced by the 4-T external magnetic field. More details of the optical spin rotation are provided in [5] and [6].

TWO-SPIN STATE PARTIAL TOMOGRAPHY

Here, we briefly outline how we are able to extract the Bell-state fidelity through a partial tomography of the two-spin density matrix, ρ. The fidelity of the state with $|\psi^{(\pm)}\rangle$ is given by $1/2 \left(\rho_{\downarrow\uparrow,\downarrow\uparrow} + \rho_{\uparrow\downarrow,\uparrow\downarrow} \pm 2\Re(\rho_{\downarrow\uparrow,\uparrow\downarrow})\right)$.

We can directly extract the spin populations $\rho_{\downarrow\uparrow,\downarrow\uparrow}$ and $\rho_{\uparrow\downarrow,\uparrow\downarrow}$ from the normalized coincidences presented in Fig. 3(a). The visibility of the transverse-basis measurements in Fig. 3(b,c), V, however corresponds to:

$$V = 2\Re\left(\rho_{\downarrow\uparrow,\uparrow\downarrow}\right) + 2\Re\left(\rho_{\downarrow\downarrow,\uparrow\uparrow}\right). \tag{2}$$

Owing to the Zeeman energy the spin states in each QD precess at $\approx 2\pi \times 25$ GHz. As such, all state coherences apart from $\rho_{\downarrow\uparrow,\uparrow\downarrow}$ and $\rho_{\uparrow\downarrow,\downarrow\uparrow}$ evolve at either $\pm 2\pi \times 25$ or $\pm 2\pi \times 50$ GHz. The timing accuracy of our measurement is given by the difference between two events: the spin rotation, which is accurate to <3 ps, and the state-projection timing, given by the superconducting nanowire single-photon detector jitter and the TDC jitter which combined are >80 ps. The latter is such that the density matrix we extract must contain the average of these fast oscillating coherences, or specifically $\Re\left(\rho_{\downarrow\downarrow,\uparrow\uparrow}\right)$ can be assumed to be zero. In this way we can directly extract $\Re\left(\rho_{\downarrow\uparrow,\uparrow\downarrow}\right)$ from the visibility of the transverse basis measurements and determine the state fidelity.

Limitations to fidelity of the created Bell states

Here, we place the fidelity we experimentally extract into context by taking into account experimental factors that contribute to its reduction. We outline how each experimental contribution reduces the maximum possible achieveable fidelity, F_{max}, from 100%. As detailed in the main text, this single photon detection scheme has an inherent limitation due to possibility of a spin-flip Raman-scattering process occuring in both QDs during a single entanglement pulse. Conditioned upon a single photon detection during the entanglement pulse, the probability of a second spin flip is p. To ensure a matched rate of photon production from both QDs (ensuring the absence of which-path information), QD A is set at $p = 0.06$ and QD B at $p = 0.08$. This represents an average contribution of double spin flip events to the final state with probability $p = 0.07$, initially leading to $F_{max} = 93\%$.

It is possible to have detected a single photon during the entanglement pulse where one of the spins was incorrectly initialized, that is, it entered the protocol in an $|\uparrow\rangle$ state. Following a photon detection, the resulting components of any output state are proportional to $|\uparrow_A\uparrow_B\rangle$. The probability of incorrect spin initialization is 3%, estimated from the proportion of remaining fluorescence at the end of the spin initialization pulses. This component reduces fidelity in the same manner as the double spin flip events, reducing both the population in the antisymmetric state and the coherence terms such that taking this into account we find $F_{max} = 90\%$.

Imperfect mode overlap at the second beam splitter of the MZI is responsible for the reduction of two-photon indistinguishability. Cases of distinguishable photons prevent the which-path information erasure required to produce the maximum fidelity Bell state. Where a photon for which the origin can be known in principle is detected this results in components of the resulting state of the form:

$$|\uparrow_A\rangle \otimes \left(\sqrt{1-p}\,|\downarrow_B\rangle + \sqrt{p}\,|\uparrow_B\rangle\right) \tag{3a}$$

$$|\uparrow_B\rangle \otimes \left(\sqrt{1-p}\,|\downarrow_A\rangle + \sqrt{p}\,|\uparrow_A\rangle\right). \tag{3b}$$

These contributions do not reduce the expected antisymmetric spin populations, and therefore the population basis measurement is unaffected. However, these components lack the coherences of a true

Bell state and reduce the rotated basis visibility of Eq. 2 by a factor of 0.93. Therefore, F_{max} is limited to 87%.

Where a Bell state has been created with F_{max} there remain limitations to the accessible fidelity due to the measurement protocol; the read-out of the spin populations itself is imperfect as revealed by Fig. S5; this results in an incorrect assignment of three-photon coincidence events with regards to the spin populations they represent, or a reduction of visibility in both the rotated basis and population basis. This is a 6% reduction, bringing F_{max} to 81%.

Finally, we must consider a second spin-state measurement error; inhomogeneous spin dephasing occurs prior to the rotation pulse causing a decrease in the measurable coherence terms of the two-spin state. By taking into account a radiative lifetime of 0.73 ns for the excited state, we estimate that 50 % of photons have been emitted by approximately 0.5 ns following the entanglement pulse. Therefore, with spin rotation occuring 0.97 ns after the peak of the entanglement photons, a typical time of spin evolution is 0.46 ns. Taking a Gaussian decay due to spin dephasing, we expect a reduction in the coherence terms (and thus the visibility of the rotated basis measurement) by a factor of 0.87 where the joint spin inhomogeneous dephasing time is 1.2 ns.

The final upper limit on the fidelity permitted by taking in to account all of these factors is $F_{max} =$ 76%. The likely source of the further reductions observed in our experiment is electrical noise in each QD sample resulting in a fluctuating phase of scattered photons (for more details see Supplementary Section 'Interference from Rayleigh scattering'). This is mapped directly on to the phase of the created Bell state, and so results in a mixing of Bell states even in the presence of a well stabilized interferometric phase. We stress that in the main text we do not present results corrected for the result of this calculation, but rather leave the results as measured.

Measurement of the two-photon visibility

The visibility of the two-photon interference can be found by comparing the coincidences at zero delay when the two inputs are parallel and perpendicularly polarized [7]. For parallel inputs photons arriving simultaneously coalesce resulting ideally in an absence of coincidences in the zero-delay peak. For perpendicularly polarized inputs, the zero delay peak is half as high as the surrounding peaks: at zero delay, coincidences arise from simultaneous arrival of photons coming from each QD while in surrounding peaks photon coincidences can also arise from successive photon emission by the same QD. The Hong-Ou-Mandel visibility, V_{HOM}, is calculated according to [7]:

$$V_{HOM} = 1 - \frac{C_\parallel(\tau = 0)}{C_\perp(\tau = 0)}, \tag{4}$$

where $C_\parallel(\tau = 0)$ is the rate of parallel polarized coincidences at zero delay and $C_\perp(\tau = 0)$ the rate for perpendicular polarized photons. Rather than measuring the non-interfering case, inaccessible in our setup due to polarization-sensitive detection, we compare the zero-delay coincidence counts to those in neighbouring peaks, where the photons are distinguishable by virtue of their arrival time. Therefore, we calculate our Hong-Ou-Mandel visibility according to:

$$V_{HOM} = 1 - 2\frac{C_\parallel(\tau = 0)}{C_\parallel(\tau \neq 0)}, \tag{5}$$

where $C_\parallel(\tau \neq 0)$ represents the average counts in the non-zero delay peaks and $C_\perp(\tau = 0) = C_\parallel(\tau \neq 0)/2$.

DATA ACQUISITION AND PROCESSING

Data acquisition

In order to correlate the detected events during the post-processing we use the TDC which takes a clock at ~ 200 kHz on the first channel and all detector events on the consecutive 4 channels and assigns them unique timestamps. The clock is generated by the AWG that controls the pulse sequence in our experiment and serves as a timing reference (for more details see Supplementary Section 'Pulse Sequence'). In order to limit the timestamp data file size we divide the measurement into intervals of one minute. The data are saved in a binary format where each event consists of 10 bins, 8 bins for the timestamp and 2 bins for the corresponding channel number. The timing resolution of the TDC is limited to 81 ps.

Data processing

Once a full minute of detection events is saved we use a Python script to process the data and extract the relevant information. In the first step every detector event is correlated to the clock in order to gain knowledge about where in the sequence an event happened. We define three regions of interest (ROIs): one for the entanglement creation (duration: 1.215 ns) and one for each read-out (duration: 6.48 ns), indicated by the grey regions in Fig. S4. Only events that occurred in one of the specified ROIs are retained and the events are separated according to the corresponding ROI they occurred in. For the entanglement ROI we only consider photon detection from the blue transition, as only a Raman photon heralds the successful creation of entanglement, whereas for the read-out events all four detectors contribute. Once all the relevant events are preselected we start to look for three-photon coincidences: we need the combination of a Raman photon to herald entanglement creation and a read-out photon from each QD to successfully determine the final spin state. The algorithm works through all events in the entanglement creation ROI and checks if there have been read-out events within the same sequence. In the case of such a successful three-photon coincidence, the timestamps as well as the spin-measurement basis are saved. Furthermore, we extract the rate of detector clicks in the different ROIs for every second of the experiment. These data are later used for the post-processing.

Post-processing

The post-processing is split up into several steps and makes use of the average detection rates extracted from the data. In Fig. S6 an example measurement of 20 minutes is presented and the different post-processing steps are indicated by the various colors. The Figure shows the entanglement rate in the upper panel and the ratio of Rayleigh scattered photons between the two interferometer outputs in the lower panel. Every point represents an interval of one second. We first check the rate of photons in the entanglement ROI and compare it to the value set prior to the experiment. Due to low-frequency (< 1 Hz) charge fluctuations in the environment, one of the two QDs occasionally wanders off resonance and we account for that by only keeping the events that occurred during a time where the rate was above a set threshold. The blue points indicate the intervals that have been discarded due to too low an entanglement rate, in the last third of the measurement the case of one quantum dot being off-resonance is quite apparent. For the measurements in the population basis this is the only post-processing performed. For the measurements of the phase of the entangled state we introduce two more post-processing steps. First we check if the additional $\pi/2$ rotations are performed correctly. This is achieved by looking at the ratio of read-out photons in the $|\uparrow\rangle$ and $|\downarrow\rangle$ states for each QD separately. For perfect rotations this
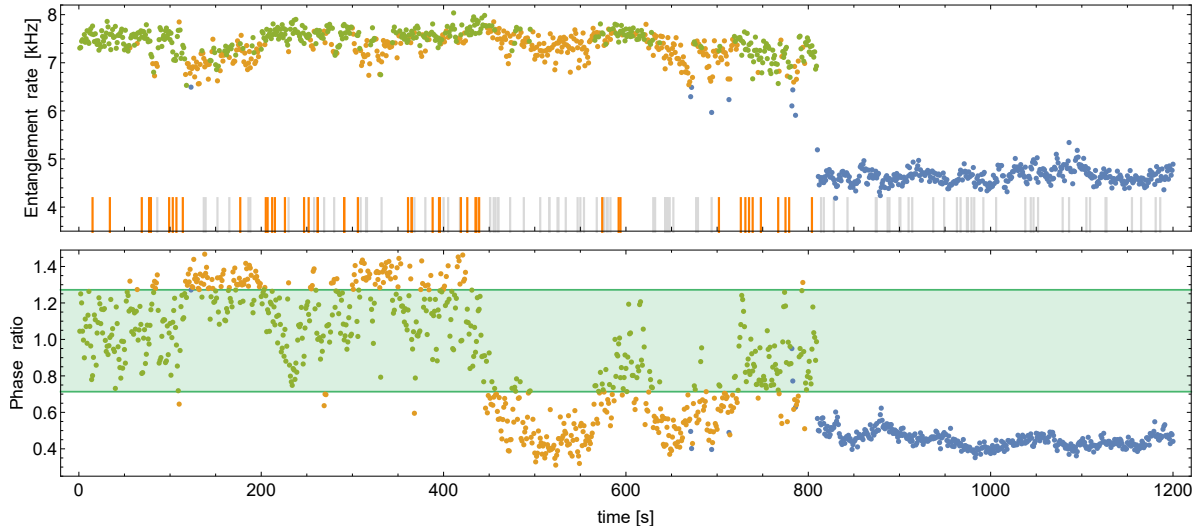
FIG. S6: Example measurement indicating the post-processing steps. The upper panel shows the entanglement rate and the lower panel the phase ratio of a 20-minute measurement. Every point indicates an interval of one second of the measurement and the colors represent the employed post-processing steps: blue points are below the entanglement threshold, orange points are ouside the interval for the phase ratio and green points are measurement intervals that fulfil all post-processing criteria. The bars in the top panel indicate all three-photon events during this measurement (N=136), where orange bars mark valid events (N=47) and grey bars mark events that did not pass the post-processing criteria (N=89). The drop in the rate for the last third of the measurement is due to one QD dropping off resonance.

ratio should be 1 and the measured value only rarely shows significant deviations, such that this step has only a negligible effect on the final result. In a final step we look at the ratio of Rayleigh-scattered photons between the two interferometer outputs within the entanglement ROI: an indication of how well the phase is maintained. The green area in the lower panel of Fig. S6 indicates the acceptance window chosen for the ratio and all intervals that did not fulfil this requirement are indicated by the orange points. The green points are all the intervals which fulfil all post-processing criteria. At the bottom of the upper panel we indicate the occurrence of three-photon coincidences by small bars; orange bars mark valid events, while grey bars indicate events that do not fulfil all post-processing criteria.

SAMPLE STRUCTURE

In Fig. S7 we present the structure of the two samples used in this work. Self-assembled InGaAs QDs are grown inside Schottky diode structure, above a distributed Bragg reflector to maximise photon outcoupling efficiency. There is a 35-nm tunnel barrier between the n-doped layer and the QDs, and a tunnel barrier above the QD layer to prevent charge leakage. The Schottky diode structure is electrically contacted through Ohmic AuGeNi contacts to the n-doped layer and a semitransparent Ti gate (6 nm) is evaporated onto the surface of the sample. The photon collection is enhanced by placement of a superhemispherical cubic zirconia solid immersion lens (SIL) on the top Schottky contact of the sample. We estimate a photon outcoupling efficiency of 10% for QDs with an emission wavelength around 970 nm.

a

GaAs
AlGaAs
AlAs
InGaAs

Si doped GaAs

Buffer and substrate

Capping (90 nm)
Tunnel barrier (50 nm)
Capping (10 nm)
QDs (2 monolayers)
Tunnel barrier (35 nm)
Back gate (40 nm)
Spacer (130 nm, 73.5 nm)
DBR (20x 82.4 nm,73.5 nm)

b

Zr SIL

Ohmic AuGeNi
contact to back gate

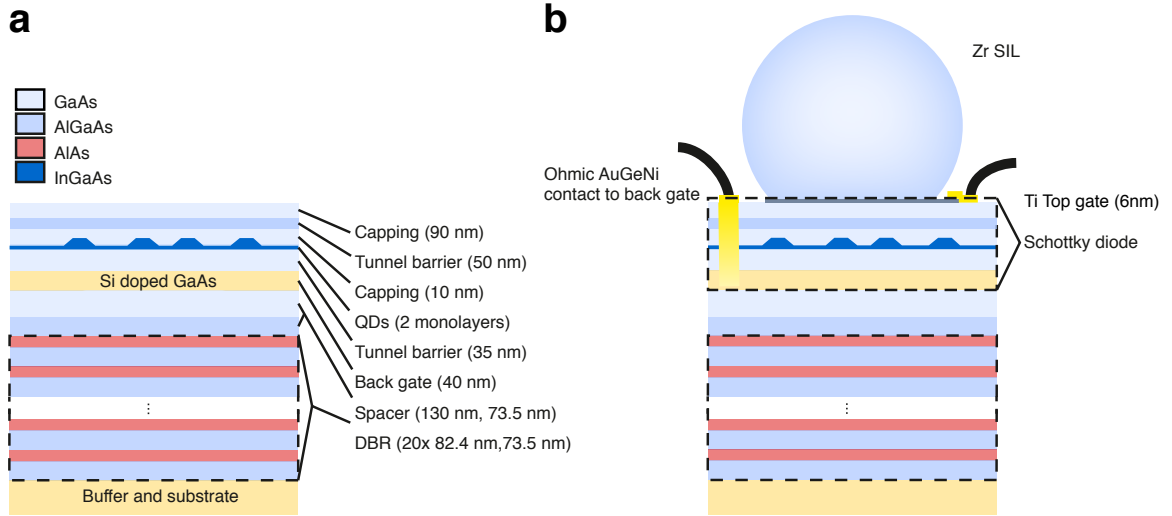Ti Top gate (6nm)

Schottky diode

FIG. S7: **a** The sample structure, indicating all MBE-grown layers. **b** Post-growth Ohmic and Schottky contacts are applied to the diode structure and a SIL is placed on the sample surface.

[1] A. V. Kuhlmann, J. Houel, A. Ludwig, L. Greuter, D. Reuter, A. D. Wieck, M. Poggio, and R. J. Warburton, Nature Physics **9**, 570 (2013).

[2] C. Matthiesen, M. J. Stanley, M. Hugues, E. Clarke, and M. Atatüre, Scientific Reports **4**, 4911 (2014).

[3] M. J. Stanley, C. Matthiesen, J. Hansom, C. Le Gall, C. H. H. Schulte, E. Clarke, and M. Atatüre, Physical Review B **90**, 195305 (2014).

[4] M. H. Levitt, Progress in Nuclear Magnetic Resonance Spectroscopy **18**, 61 (1986).

[5] D. Press, T. D. Ladd, B. Zhang, and Y. Yamamoto, Nature **456**, 218 (2008).

[6] R. Stockill, C. Le Gall, C. Matthiesen, L. Huthmacher, E. Clarke, M. Hugues, and M. Atatüre, Nature Communications **7**, 12745 (2016).

[7] E. Flagg, A. Muller, S. Polyakov, A. Ling, A. Migdall, and G. Solomon, Physical Review Letters **104**, 137401 (2010).